• Original Paper •

Atmospheric Warming Slowdown during 1998-2013 Associated with Increasing Ocean Heat Content

Changyu LI , Jianping HUANG* , Yongli HE , Dongdong LI , and Lei DING

Key Laboratory for Semi-Arid Climate Change of the Ministry of Education, *College of Atmospheric Sciences*, *Lanzhou University*, *Lanzhou*, *Gansu* 730000, *China*

ABSTRACT

Although atmospheric greenhouse gas concentrations continuously increased, there was relatively little change in global-averaged surface temperatures from 1998 to 2013, which is known as atmospheric warming slowdown. For further understanding the mechanism involved, we explored the energy redistribution between the atmosphere and ocean in different latitudes and depths by using data analysis as well as simulations of a coupled atmosphere–ocean box model. The results revealed that, compared with observational changes of ocean heat content (OHC) associated with rapid warming, the OHC changes related to warming slowdown are relatively larger in multiple ocean basins, particularly in the deeper layer of the Atlantic. The coupled box model also showed that there is a larger increasing trend of OHC under the warming slowdown scenario than the rapid warming scenario. Particularly, during the warming slowdown period, the heat storage in the deeper ocean increases faster than the ocean heat uptake in the surface ocean. The simulations indicated that the warming patterns under the two scenarios are accompanied by distinct outgoing longwave radiation and atmospheric meridional heat transport, as well as other related processes, thus leading to different characteristics of ocean heat uptake. Due to the global energy balance, we suggest this slowdown has a tight relationship with the accelerated heat transport into the global ocean.

Key words: warming slowdown, ocean heat content, box model, heat transport

Article Highlights:

• The atmospheric warming slowdown is closely coupled with the accelerated heat transport into the global ocean.
• Observed decadal variability of OHC shows a tight relationship with atmospheric temperature change.
• The coupled box model demonstrated the differences of energy transport in the climate system between the warming slowdown and rapid warming period.

---

1. Introduction

As a result of industrialization, the carbon dioxide in the Earth's atmosphere has increased continuously over the past 100 years, which is considered as the main reason behind global warming (IPCC, 2013). However, the global mean atmospheric temperature (especially in the surface layer) leveled off over the first decade of the 21st century, in contrast to the rapid warming during the late 20th century (Fig. 1). This phenomenon has been referred to as an atmospheric warming slowdown or hiatus (e.g., Easterling and Wehner, 2009; Foster and Rahmstorf, 2011; Meehl et al., 2011; England et al., 2014; Guan et al.,

2015; Steinman et al., 2015; Huang et al., 2017, He et al., 2018), and has attracted great attention worldwide owing to its ostensible contradiction of the human-induced global warming theory (Otterå et al., 2010).

Improving comprehension of the atmospheric warming slowdown can provide a better projection of future climate (Yao et al., 2017), and the energy balance of the climate system may help us further understand the mechanism behind the phenomenon (Trenberth et al., 2014a). According to observations, greenhouse gases (GHGs) have continued to increase in the 21st century (WMO, 2014), which means that the radiative forcing induced by GHGs is increasing and the energy continued to be trapped in Earth's climate system during the atmospheric warming slowdown. Thus, there must have been a redistribution of heat from the atmosphere to elsewhere in the climate system to

---

* Corresponding author: Jianping HUANG
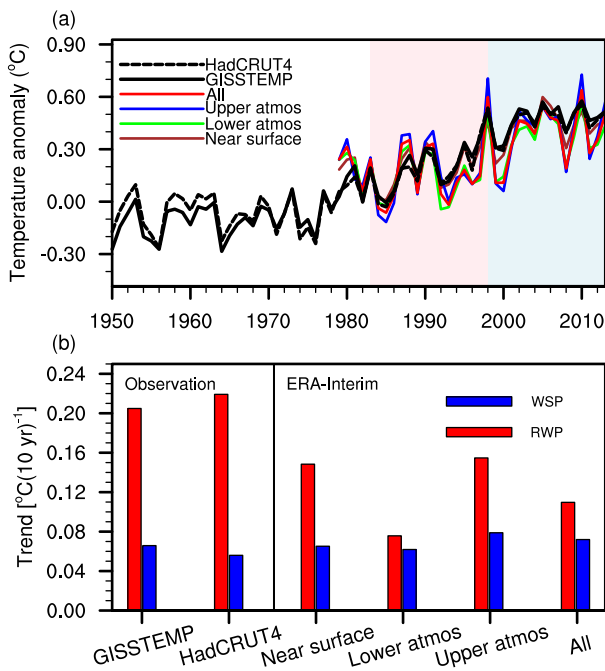 Email: hjp@lzu.edu.cn

Fig. 1. Time series of the global mean temperature anomaly relative to the climatology of 1961–90 (a) and trends of global mean temperature for 1983–98 (RWP, red) and 1998–2013 (WSP, blue) (b). The black solid and dashed lines represent the surface temperature derived from GISSTEMP and HadCRUT4, respectively. The colored lines represent the atmospheric temperature derived from ERA-Interim for the near surface (brown), lower atmosphere (green, from the surface to 500 hPa), upper atmosphere (blue, from 500 hPa to 100 hPa), and the whole atmosphere (red, from the surface to 100 hPa).

fit the slowdown of the atmospheric warming. This points toward the vital role played by the ocean in this slowdown owing to its huge heat capacity, and, more importantly, there is a continuous "global warming" if we focus on the whole climate system rather than just the atmosphere (Cheng et al., 2018). Indeed, many studies have suggested that the oceanic decadal modes, which are tightly linked to the changes in ocean heat content (OHC), may be the main cause of the atmospheric warming slowdown. Kosaka and Xie (2013) concluded that the current warming slowdown is tied specifically to La-Niña-like decadal cooling in the Pacific, induced by accelerated trade winds. Some researchers suggest that the phenomenon occurs during the negative phase of the Pacific Decadal Oscillation, or the Interdecadal Pacific Oscillation, which can broadly explain the Pacific OHC changes in the slowdown period (Trenberth and Fasullo, 2014b; Dai et al., 2015). Besides, the Atlantic Multidecadal Oscillation has been proposed as a predictor or key factor for the mean surface temperature over the Northern Hemisphere or globe (Wyatt et al., 2012; Chylek et al., 2014). The atmospheric teleconnection over the Atlantic is generally represented by the North Atlantic Oscillation, which has been suggested to have contributed to the recent warming slowdown (Guan et al., 2015). Huang et al. (2017) suggested that these internal climate variability modes can excite a decadal modulated oscillation, which can explain up to 95% of the temperature variance

in the boreal cold season over the continental Northern Hemisphere during the warming slowdown. Furthermore, Liu and Zhou (2017) explored the atmospheric footprint of the warming slowdown, and found it to be coupled with changes in the air–sea latent heat flux. Chen and Tung (2014) also proposed that the warming slowdown may have been caused by oceanic heat transport.

Although the warming slowdown has been partially explained well by internal climate variability, its physical mechanism still needs to be further studied. In this study, the characteristics of atmospheric warming slowdown are explored from the global energy balance perspective. We investigate the energy redistribution between the atmosphere and ocean in different latitudes and depths based on analysis of observations, reanalysis products, and the simulations of a coupled atmosphere–ocean box model. We attempt to provide a better understanding of the oceanic energy transport and reveal the fundamental factors that influence this process.

The paper is arranged as follows. Section 2 describes the details of the datasets and the methodology. Section 3 introduces the coupled atmosphere–ocean box model used in this study. The characteristics of the atmospheric temperature anomaly and OHC anomaly related to the warming slowdown period (WSP) and rapid warming period (RWP) are presented in section 4. Section 5 examines the heat transport between the atmosphere and ocean at different depths and latitudes during the WSP and RWP in the box model. Discussion and conclusions are presented in section 6.

2.   Data and methods

2.1.   *Data sources*

The analysis of OHC was based on the Institute of Atmospheric Physics (IAP) gridded ocean temperature dataset and the ECMWF's Ocean Reanalysis System 4 (ORAS4) dataset. The IAP dataset features global coverage of the oceans at 41 vertical levels from the surface to 2000 m, and monthly temporal resolution from 1940 to present (Cheng et al., 2016, 2017). The ORAS4 dataset, which assimilates a variety of observational information in an ocean model (Balmaseda et al., 2013), extends to a depth of 5000 m, but only 0–2000 m is used here to compare with the IAP dataset. The analysis of global surface temperature was based on the GISTEMP and HadCRUT4 datasets. The GISTEMP dataset, which consists of global surface temperature and covers the period from 1880 to the present day (Hansen et al., 2010), was used to calculate the linear trend of the surface temperature, and HadCRUT4 (Morice et al., 2012) was used for comparison with GISTEMP. The analysis of air temperature for the whole atmosphere was based on ERA-Interim (Dee et al., 2011).

2.2.   *Ensemble Empirical Mode Decomposition method*

The Ensemble Empirical Mode Decomposition (EEMD) method was used in our study. It is an adaptive 1D data analysis method that can reflect the nonlinear and nonstationary nature of climate data. Therefore, by using this method, the cli-

mate variability can be split into different oscillatory components with intrinsic time scales, including interannual, decadal, and multidecadal extents. In this article, the steps of EEMD were taken from Ji et al. (2014) and Huang et al. (2017), which are described in detail in the Supplementary Material.

2.3. *Division of the ocean*

In this study, the ocean was divided into five regions: the Pacific Ocean, Atlantic Ocean, Indian Ocean, Southern Ocean, and others. The Southern Ocean was separated from other basins by 35°S, and the boundary between the Indian Ocean and the Pacific Ocean was 120°E. The ranges of each ocean basin are presented in Fig. S1 in Electronic Supplementary Material.

3. Coupled atmosphere–ocean box model

A coupled atmosphere–ocean box model was used in this study to investigate the characteristics of energy transport in the climate system during the RWP and WSP. It takes regional differences by latitude into consideration and divides the atmosphere and ocean into a small number of isothermal reservoirs. The ocean model is based on Schneider and Thompson (1981) and further developed in Harvey and Schneider (1985). Detailed derivations can be found in these publications.

In the model, the atmosphere has only one layer and is divided into two boxes; the ocean has three layers—namely, the upper layer, intermediate layer, and bottom layer—and each layer is also divided into two boxes (Fig. 2). There is heat transport among these boxes of the atmosphere–ocean system. The boxes at low latitude and those at high latitude are linked at 35°N, where the zonal-mean net radiative forcing is close to zero and the poleward atmospheric heat transport is near its peak (Nakamura et al., 1994). The zonal-mean net radiative forcing is positive (negative) over the south (north) of 35°N. The equations for this system are as follows:

$$C_{A1}\frac{dT_{A1}}{dt} = A_1 - B_1 T_{A1} - \chi(T_{A1} - T_{A2}) - R_1 + F_1 ; \quad (1)$$

$$C_{A2}\frac{dT_{A2}}{dt} = A_2 - B_2 T_{A2} + \chi(T_{A1} - T_{A2}) - R_2 + F_2 ; \quad (2)$$

$$C_{U1}\frac{dT_{U1}}{dt} = R_1 + C_w \frac{D_U}{\tau}(T_{I1} - T_{U1}) + C_w \frac{\dot{V}}{\sigma}(T_{I1} - T_{U1}) ; \quad (3)$$

$$C_{U2}\frac{dT_{U2}}{dt} = R_2 + C_w \frac{D_U}{\tau}(T_{I2} - T_{U2}) + C_w \frac{\dot{V}}{\sigma}(T_{U1} - T_{U2}) ; \quad (4)$$

$$C_{I1}\frac{dT_{I1}}{dt} = -C_w \frac{D_U}{\tau}(T_{I1} - T_{U1}) + C_w \frac{\dot{V}}{\sigma}(T_{B1} - T_{I1}) ; \quad (5)$$

$$C_{I2}\frac{dT_{I2}}{dt} = -C_w \frac{D_U}{\tau}(T_{I2} - T_{U2}) + C_w \frac{\dot{V}}{\sigma}(T_{U2} - T_{I2}) ; \quad (6)$$

$$C_{B1}\frac{dT_{B1}}{dt} = C_w \frac{\dot{V}}{\sigma}(T_{B2} - T_{B1}) ; \quad (7)$$

$$C_{B2}\frac{dT_{B2}}{dt} = C_w \frac{\dot{V}}{\sigma}(T_{I2} - T_{B2}) . \quad (8)$$

Here, T_A, T_U, T_I and T_B represent the temperature of the atmosphere, the upper layer ocean, the intermediate layer ocean, and the bottom layer ocean, respectively; C_A, C_U, C_I and C_B are the corresponding heat capacities, which are equal to the depth of each ocean layer multiplied by the heat capacity of a unit of water; A is the net incoming radiation and B is the climate feedback parameter, where $A - B T_A$ represents the net radiative forcing at the top of atmosphere; F is the human-induced radiative forcing; R represents the energy exchange occurring at the surface of the ocean, the perturbation of which is of vital importance in our study and will be discussed in detail below; D_U is the depth of the upper layer ocean and C_w is the volumetric heat capacity of water; τ is the turnover time of upper-layer water with intermediate layer water; $\dot{V}$ is the thermohaline mass flux and σ is the area of the ocean; χ is the efficiency of atmospheric heat transport. The subscript "1" represents the low latitudes and the subscript "2" represents the high latitudes. All parameters used in this study are listed in Table 1. Their values are based on previous box-model studies (Schneider and Thompson, 1981; Danny Harvey and Schneider, 1985; Marotzke and Stone, 1995; Krasovskiy and Stone, 1998; Yang et al., 2016).

The equilibrium states of the box model can be obtained by setting all of the time derivations to zero ($dT_i/dt = 0$ for each box). For the atmosphere, we obtain:

$$A_1 - B_1 T_{A1} - \chi(T_{A1} - T_{A2}) - R = 0 ; \quad (9)$$

$$A_2 - B_2 T_{A2} + \chi(T_{A1} - T_{A2}) + R = 0 . \quad (10)$$

Note that we do not take the human-induced radiative forcing F into consideration now. According to the values listed in Table 1, we can determine the equilibrium states of the model. The temperature of the atmosphere is 28.2 °C in low latitudes (T_{A1}) and 1.2 °C in high latitudes (T_{A2}), with a global-averaged temperature ($\frac{T_{A1} + T_{A2}}{2}$) of 14.7 °C. The meridional temperature contrast is equal to 27.0 °C, which is consistent with the result of Yang et al. (2015). However, it should be emphasized that the temperature of some ocean boxes becomes the same when the model reaches the equilibrium state ($T_{U2} = T_{I2} = T_{B1} = T_{B2}$). Thus, the model is often used to study the response (the perturbation) to external forcing rather than the final state of the climate system.

Now let us proceed to consider the response (or the perturbation) of the system to the human-induced greenhouse effect. We assume that the concentration of CO_2 increases linearly with time (Kim et al., 1992), and its radiative forcing can be expressed as
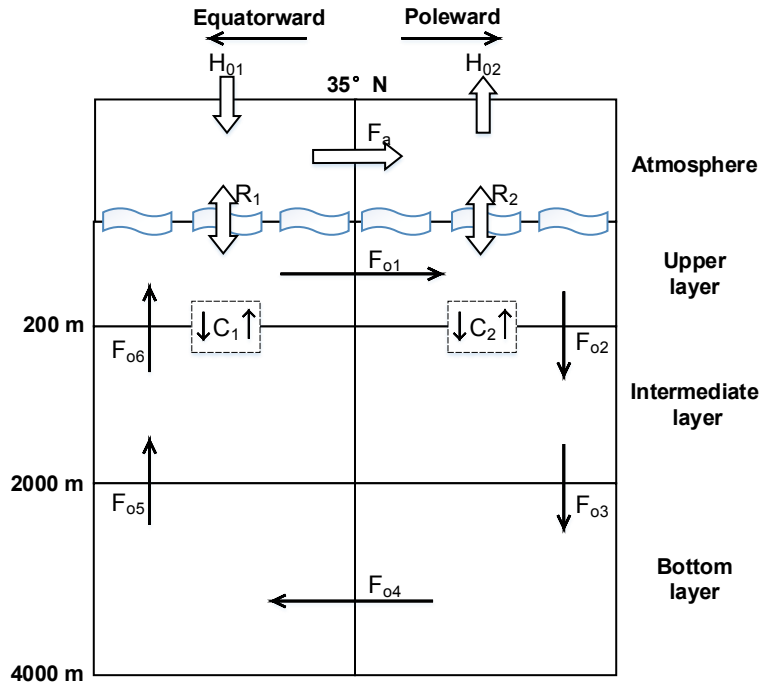
$$\Delta F = rtH(t) , \quad (11)$$

Fig. 2. Schematic plot of the coupled atmosphere–ocean box model. H_0 is the net energy gains at the top of the atmosphere; R represents the energy exchange occurring at the surface of the ocean; F_{o1}–F_{o6} illustrate qualitatively the heat transports among different ocean boxes; F_a is the meridional atmosphere energy transport.

Table 1. Parameters used in the box model.

Symbol	Physical meaning	Value	Notes
C_w	Heat capacity of a unit of water volume	4×10^6 J m^{-3} K^{-1}	—
A_1	Net incoming energy in low latitudes	90 W m^{-2}	Marotzke
A_2	Net incoming energy in high latitudes	−40 W m^{-2}	—
B	Climate feedback parameter	1.7 W m^{-2} K^{-1}	Marotzke
D_U	Depth of upper layer	200 m	—
D_T	Depth of intermediate layer	2000 m	—
D_B	Depth of bottom layer	4000 m	—
R_0	Equilibrium air–sea energy exchange	6.9 W m^{-2}	—
τ	Turnover time of upper-layer water	10 yr	Harvey
$\dot{V}$	Thermohaline mass	4.84×10^7 m^3 s^{-1}	Harvey

$$H(t) = \begin{cases} 0, t < 0 \\ 1, t \geq 0 \end{cases}, \qquad (12)$$

where $r = 0.03$ W m^{-2} yr^{-1}, which is equivalent to the greenhouse effect caused by a doubling of the CO_2 concentration in 140 years; $H(t)$ represents the impulse function; t represents the time. The additional heat into the climate system as a result of the greenhouse effect can be calculated using Eq. 11 and 12.

There is another key point when we calculate the perturbation of energy transport after taking CO_2 forcing into consideration, and that is how to deal with the heat uptake in the air–sea interface (ΔR). Previous studies have proposed many parameterizations of the energy transport at the Earth's sea surface (Warren and Schneider, 1979; Danny Harvey and Schneider, 1985; Morantine and Watts, 1990), but it seems quite difficult to repro-

duce the warming slowdown with these schemes. Besides, although over 90% of this positive energy imbalance is manifested in increased OHC (von Schuckmann et al., 2016), there is still not enough clarity about how the heat is taken into the ocean, due to large uncertainty in observational air–sea heat flux (Josey, 2011). In this case, we handle it on the basis of energy conservation rather than applying these schemes. The purpose of the box model is to investigate the characteristics of energy transport in the climate system during the WSP, so we directly fix the change rate of atmospheric temperature, which is derived from ERA-Interim during the WSP (shown in Fig. 3c), in the box model. The changes of corresponding atmosphere heat content can thus be calculated. Due to the energy conservation of the model atmosphere–ocean system, we can now get the OHC change under the warming slowdown scenario by subtracting the atmosphere's heat content change from the total in-

creased energy of the model atmosphere–ocean system. Similarly, the characteristics of heat distribution in the system under the rapid warming scenario can also be investigated with this method.

Assume any variable can be expressed as $A+\Delta A$, where A is the equilibrium state and ΔA is the perturbation. Considering Eqs. (9) and (10), the functions of perturbation in the model system (only the equations of the atmosphere part are shown here) can be written as

$$C_{A1}\frac{d(\Delta T_{A1})}{dt} = -B_1\Delta T_{A1} - \chi(\Delta T_{A1} - \Delta T_{A2}) - \Delta R_1 + \Delta F_1 \,, \tag{13}$$

$$C_{A2}\frac{d(\Delta T_{A2})}{dt} = -B_2\Delta T_{A2} + \chi(\Delta T_{A1} - \Delta T_{A2}) - \Delta R_2 + \Delta F_2 \,, \tag{14}$$

where the terms in Eqs. (13) and (14), from left to right, represent the change of atmospheric heat content, the climate feedback, the meridional atmospheric heat transport, the ocean heat uptake, and the radiative forcing, respectively. The ocean heat uptake or the energy transported into the ocean can be easily determined according to the given change in atmospheric temperature.

4. Change in atmospheric temperature and OHC

The characteristics of both the global atmospheric temperature anomaly and OHC anomaly during the WSP are evidently different from those during the RWP.

For the atmosphere, both observational datasets (GISTEMP and HadCRUT4) show that the warming trends of the global mean surface temperature anomaly during the WSP are obviously smaller than those during the RWP (Fig. 1b). The characteristics of the atmospheric temperature anomaly derived from ERA-Interim are consistent with the two observational datasets, though their amplitudes have some differences. It is apparent that the whole atmosphere (from the surface up to 100 hPa) experiences a warming slowdown in the 21st century, compared with the rapid warming in the 1980s and 1990s (Fig. 1; details of atmospheric temperature trend distribution in different pressure levels shown in Fig. S2). Comparing the trends of atmospheric temperature during the two periods, it is evident that the atmosphere accommodates less heat in the WSP than the RWP: while the atmospheric heat content in total increases about 0.62×10^{21} J in the period of the warming slowdown, this increase is much less than that in the RWP (approximately 1.37×10^{21} J), which reveals the different features of heat transport between the two periods.

The shift in heat transport in the climate system can also be demonstrated by the trends of zonal mean atmospheric temperature (pressure versus latitude) during the RWP and WSP, which are shown in Fig. 3. It can be seen that the vertical distributions of the zonal mean temperature trend are obviously different between the two periods (Figs. 3a and b). The low-latitude

atmosphere shows an apparent warming trend from the surface to around the 150 hPa level during the RWP; however, this warming trend weakens or even becomes negative during the WSP. As for the high latitudes, significant cooling is in the upper atmosphere during the RWP, but this cooling weakens over the Arctic regions and even becomes warming over the Antarctic during the WSP. The spatial distribution of the temperature trend in each pressure level can be found in Fig. S2. Overall, in the high latitudes, the atmosphere warms even faster during the WSP than during the RWP; whereas, in the low latitudes, the warming trend during the WSP shows a sharp decline, compared with the warming trend during the RWP (Fig. 3c). These results indicate that the atmospheric temperature trend in the low latitudes contributes most to the warming slowdown, and more importantly, changes in heat transport in the climate system occur during the two periods.

Figure 4 presents the time series of OHC in the global ocean and each ocean basin, from which continuous rapid increases in OHC since the 1980s due to the growth of greenhouse gasses (GHGs) can be seen. This GHG-forced long-term warming can also be found in the reanalysis dataset ORAS4 (Fig. S3), though it suffers from discontinuity due to an upgrading of the oceanic observation system (Palmer et al., 2017). That is, the substantial anthropogenic warming (GHG-forced) signal in the OHC records should be removed before investigating OHC changes related to the slowdown (i.e., natural variability of OHC). Here, we used the EEMD method, proposed by Wu and Huang (2009) and Ji et al. (2014), to separate the decadal variability from the long-term anthropogenic warming. Based on this method, we were able to decompose the atmospheric temperature anomaly and OHC anomaly into different time scales. As shown in Fig. 5, there are two main components in both OHC and atmospheric temperature series: a decadal to multidecadal oscillation (Figs. 5a and b), and the long-term upward trend (Figs. 5c and d). The long-term trend is considered to be mainly contributed by the radiative forcing (Wu et al., 2011; von Schuckmann et al., 2016; Huang et al., 2017). The oscillation component, which represents the natural variability, enhances or suppresses the long-term trend on decadal to multidecadal time scales. For the OHC, when the oscillation is in a downward phase (Fig. 5a), which means less heat uptake in the ocean, it contributes to an accelerated warming trend in atmospheric temperature, as in the 1990s (Fig. 5b). There is an upward swing in the oscillation of OHC in 1995–96 (Fig. 5a), and thus a subsequent downward phase of the atmospheric temperature oscillation since about 2002 (Fig. 5b), which reduces the long-term upward trend in atmospheric temperature and ultimately results in the recent surface warming slowdown (Fig. 5f). It should be noted that the response of atmospheric temperature to the OHC increase seems to have a lag in time (~5 years; Figs. 5a and b). The downswing of OHC arises in 2006–07 and, after about 5 years, the atmospheric warming slowdown comes to an end with an upswing of atmospheric temperature. Similar results about this lag can also be found in Chen and Tung (2018), when they discussed the relationship between the warming slowdown and Atlantic Overturning Circulation. The
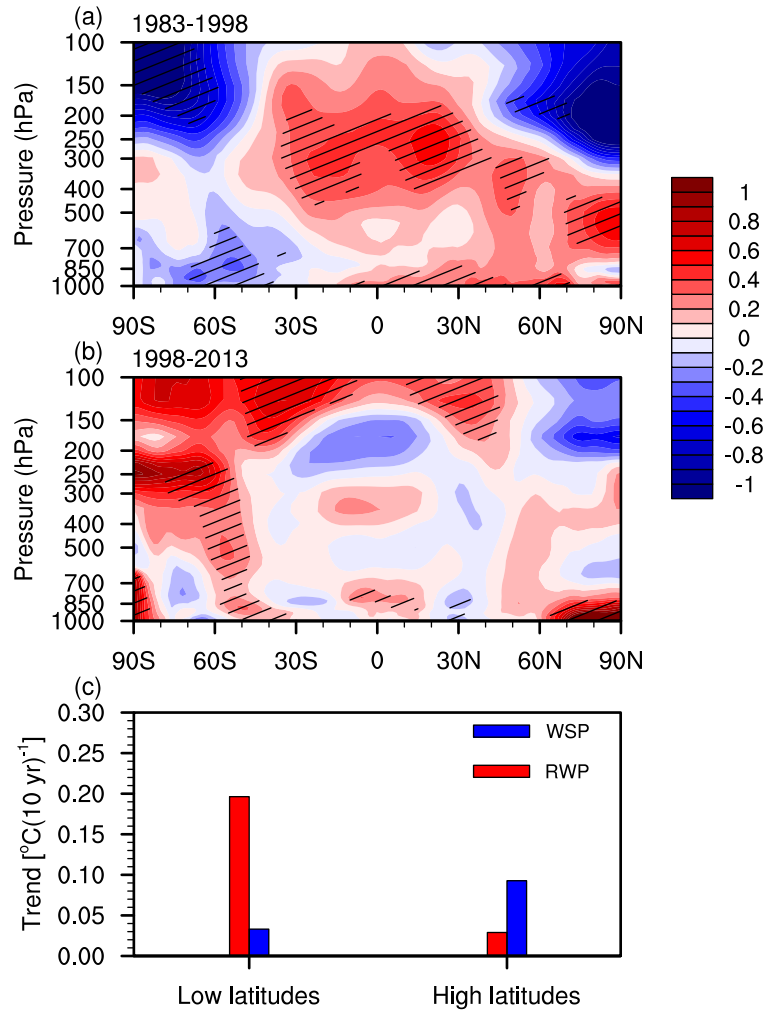
Fig. 3. Trend of zonal-mean atmospheric temperature during the (a) RWP (1983–98) and (b) WSP (1998–2013) derived from ERA-Interim. Trends for the atmosphere in low and high latitudes (divided by 35°N) in the two periods are shown in (c). Shaded zones are statistically significant at the 5% level.

sensitivity of the EEMD to the time period selected was also examined, and the results showed the time period has little impact on the pattern of the oscillation component of OHC (Fig. S4).

The characteristics of OHC differ in different ocean basins (Fig. 4), which indicates the contribution of each ocean basin to the warming slowdown may be different (Yao et al., 2017). Therefore, to remove the long-term anthropogenic warming signal, as well as quantify the contribution of each ocean basin to the warming slowdown, we applied the "Trend-Diff method", which was proposed in Cheng et al. (2018), to each ocean basin with different depths. This method uses the trend differences to reduce the impact of the substantial warming signal, assuming the long-term warming rate is constant in the research period. Although there should be an acceleration of long-term warming (non-constant in rate) due to the accumulation of GHGs, this method shows similar results with analysis of the non-constant trend proposed in Trenberth and Shea (2006), and is thus acceptable, as mentioned in Cheng et al. (2018). Due to the 5-year prior phase of OHC shown in the EEMD (Figs. 5a and b), the trend differences were calculated between the years

1993–2008 (period of OHC decadal variability related to warming slowdown) and 1979–92 (period of OHC decadal variability related to rapid warming), and the oceans were divided into two layers vertically: the upper layer (0–200 m) and the deeper layer (200–2000 m). The results are shown in Table 2. It can be seen that both the upper and deeper layer in the Atlantic, Pacific and Indian oceans present a positive trend difference, while the Southern Ocean makes a negative contribution. According to the calculations, the largest trend differences exist in the Atlantic, especially its deeper layer (~2.44 × 10^{21} J yr^{-1}; > 70% in the deeper layer), followed by the Indian and Pacific oceans, with trend differences of ~2.08 × 10^{21} J yr^{-1} and 1.69 × 10^{21} J yr^{-1}, respectively. The global trend of OHC in 1993–2008 in total increases about 5.15 × 10^{21} J yr^{-1} compared with the reference period 1979–92, and the deeper ocean (below 200 m) contributes about 60% of the total. The results indicate that more heat is transported to the deeper ocean, such as the deeper layer of the Atlantic.

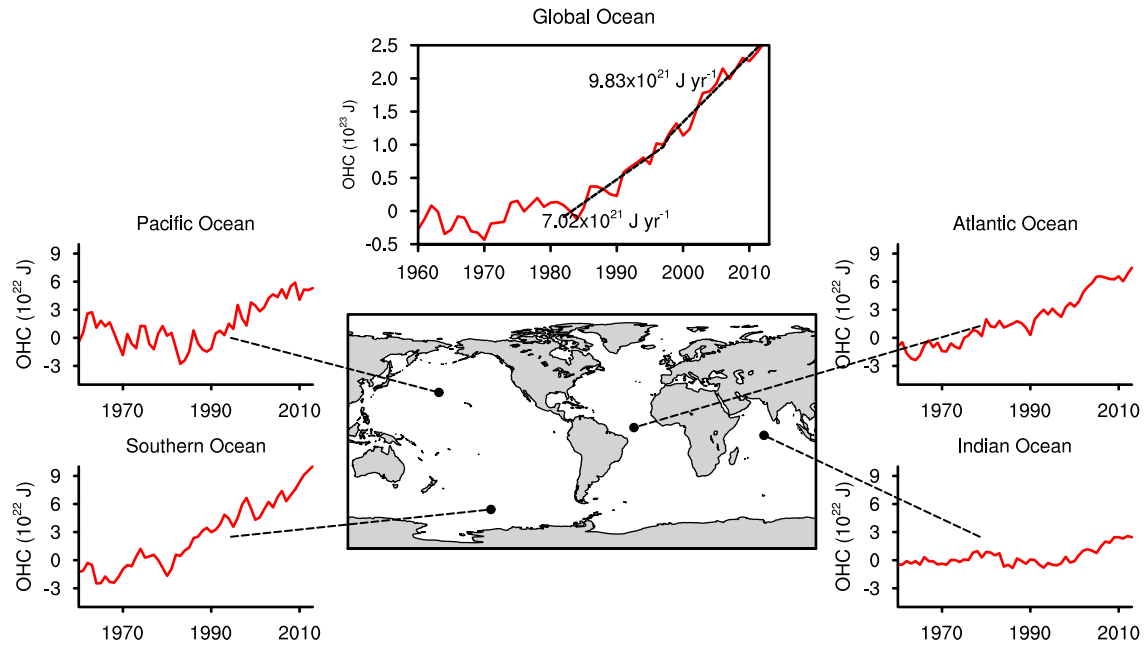For further investigation, EOF analysis of the detrended OHC was also applied to each layer. The results are shown in

Global Ocean

9.83×10^{21} J yr^{-1}

7.02×10^{21} J yr^{-1}

OHC (10^{23} J)

Pacific Ocean

OHC (10^{22} J)

Atlantic Ocean

OHC (10^{22} J)

Southern Ocean

OHC (10^{22} J)

Indian Ocean

OHC (10^{22} J)

Fig. 4. The OHC anomaly (red) averaged in the global ocean, Atlantic Ocean, Southern Ocean, Pacific Ocean, and Indian Ocean, relative to the climatology from 1961 to 1990 based on the IAP dataset. The dashed lines represent the linear trend of OHC during 1983–98 and 1998–2013, respectively.

OHC

$\times10^{23}$

(a) Oscillation

(c) Long-trem trend

(e) Trend + Oscilliation

Year

Atmospheric temperature

(b)

(d)

(f)

Year
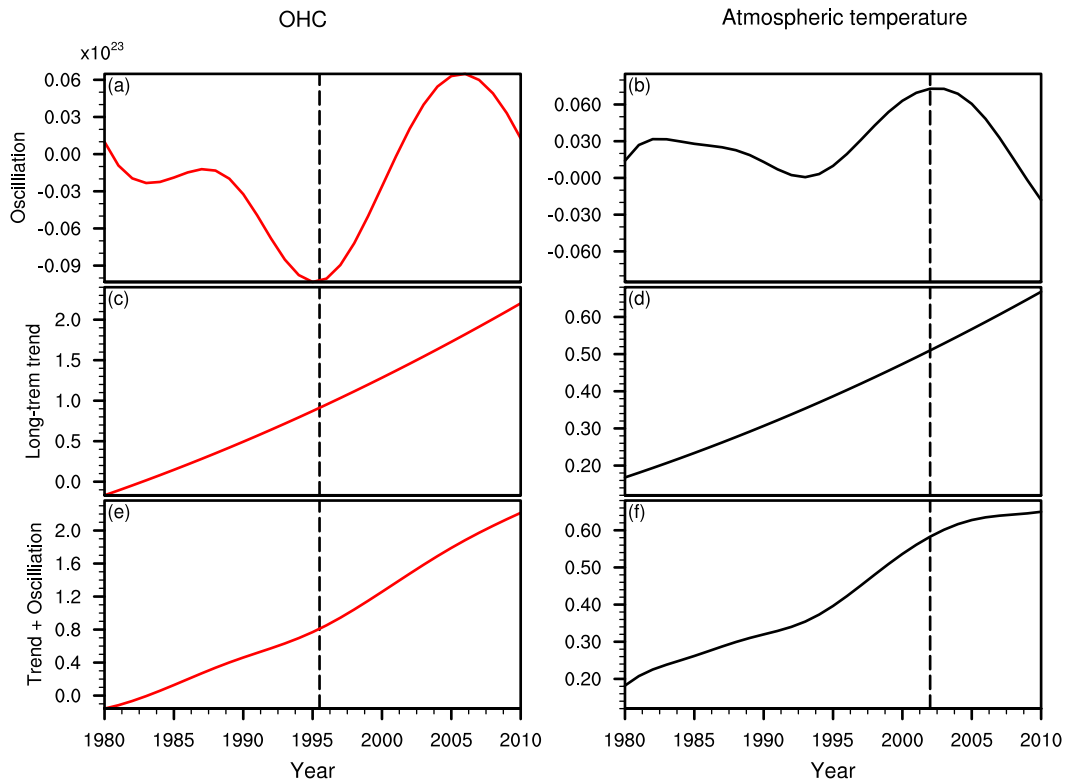
Fig. 5. EEMD global annual mean OHC from the IAP dataset (red, from the sea surface to 2000 m depth) and atmospheric temperature from GISSTEMP (black) anomalies for the oscillation component (a, b), long-term trend component (c, d), and the trend plus oscillation (e, f). The oscillation component is the sum of IMF (intrinsic mode function) 3, 4 and 5 from the EEMD, and the long-term trend is IMF 6. We mainly focus on the decadal and the multidecadal time scales, so IMF 1 and 2 are ignored, which represents high-frequency oscillation.

Fig. 6. After removing the linear trend from the OHC series, the EOF analysis for the OHC of the upper layer ocean showed that the spatial pattern of the first leading mode (EOF1), which explains about 33% of the total variance, is mainly characterized in the tropical Pacific, and has an east–west structure (Fig. 6a). The time series (PC1) associated with EOF1 changes to a negative trend from 1998 when the warming slowdown occurs, while it persists in a positive trend during the 1980s and 1990s (Fig. 6c). This pattern, which has a close relationship (correlation coefficient of ~0.91; significant at the 0.01 level) with Oceanic Niño Index, indicates the important role of ENSO in the modulation of OHC in the upper ocean. Consistent with the EOF analysis, the trend differences of OHC in the Pacific Ocean mainly occur within a shallow layer and in the east–west direction (Figs. S5a and b), with an opposite pattern between the RWP and WSP. As for the deeper layer ocean, EOF1 explains about 15% of the total variance, and the positive patterns of OHC changes in the deeper layer are mainly located in the Atlantic and the Indian Ocean (Fig. 6b). PC1 shows a downward trend in the 1980s–90s and a subsequent upward trend at the end of the 20th century (Fig. 6d). This indicates that there is a positive OHC anomaly associated with the warming slowdown and a negative OHC anomaly associated with the rapid warming, suggesting more heat is stored in the deeper layer ocean during the WSP than during the RWP (also shown in the trend differences of the OHC anomaly in the Atlantic basin in Figs. S5c and d). The increase of Atlantic OHC in EOF1 was also found by Lee et al. (2011) and Chen and Tung (2014).

These characteristics of OHC described above reflect the different mechanisms of OHC redistribution in the ocean basins. The thermohaline circulation plays an important role in the Atlantic (Rahmstorf, 2002). Therefore, the OHC anomaly contributed by the Atlantic is mainly in the deeper layer (Table 2, Fig. 6c); whereas, heat redistribution in the upper 200 m in the Pacific is strongly influenced by ENSO (Fig. 6a). The OHC changes in the Indian Ocean are dominated by the Indonesian Throughflow, the increases of which could be responsible for the positive OHC trend differences shown in Table 2 (Lee et al., 2015; Li et al., 2017).

Table 2. OHC trend differences between two periods (1993–2008 minus 1979–92).

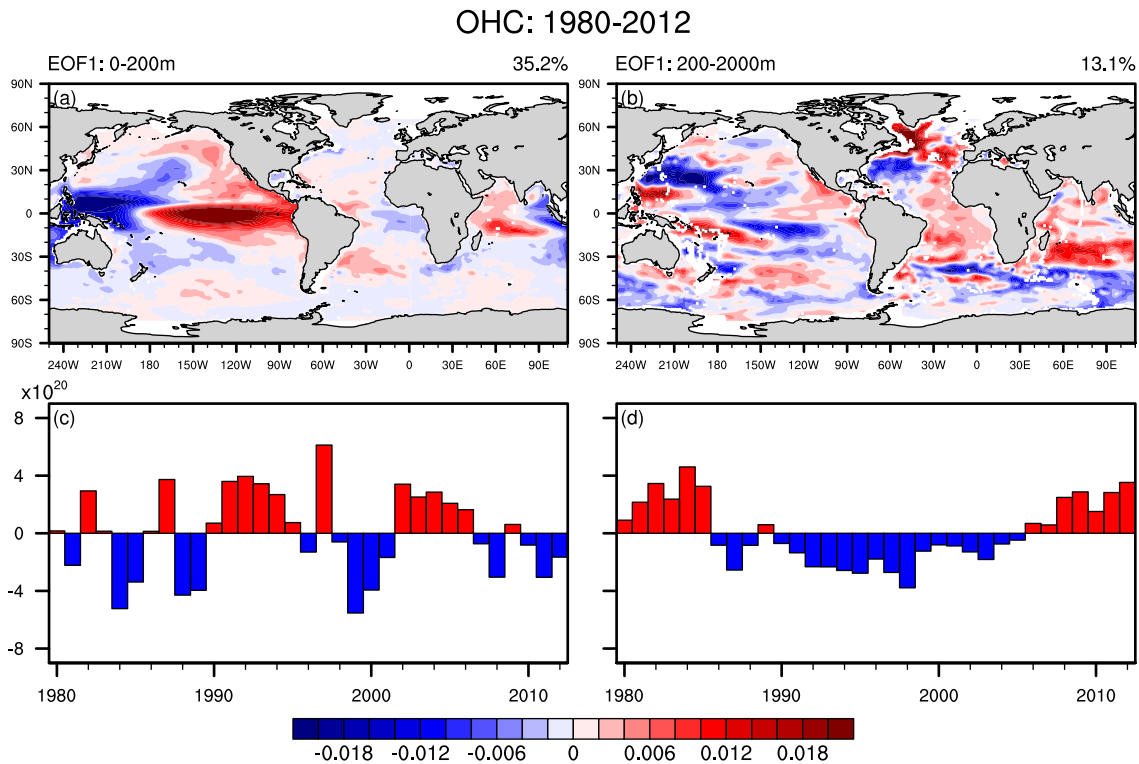| (10^{21} J yr^{-1})	Pacific Ocean	Atlantic Ocean	Southern Ocean	Indian Ocean	Others	Total
Upper 200 m	0.66	0.68	−0.08	0.73	0.12	2.11
Below 200 m	1.03	1.76	−1.33	1.35	0.23	3.04
Total	1.69	2.44	−1.41	2.08	0.35	5.15

Fig. 6. First EOF mode of the detrended OHC in the upper layers (0–300 m) (a) and the deeper layers (300–2000 m) (b). The PC1 time series associated with the EOF mode are shown in (c) and (d) for the upper layers and deeper layers, respectively. The percentage of variance explained by each mode is indicated in the right-hand corner. The second EOF modes and their associated PC2 time series are not shown. The observational OHC is based on the IAP dataset.

In summary, we found that the whole atmosphere (from the surface to 150-hPa level), particularly the low-latitude atmosphere, shows an obvious warming slowdown during the WSP (1998–2013) compared with that during the RWP (1983–98). After removing the long-term anthropogenic warming signal (forced by GHGs), we found that the global changes of OHC related to the atmospheric warming slowdown increase faster than its changes in the reference period related to rapid warming, particularly the OHC in the deeper layer (200–2000 m) of the Atlantic and Indian Ocean. From the global energy balance perspective, we suggest that the recent global atmosphere warming slowdown is closely coupled with the faster increasing of global OHC.

5. OHC anomaly simulated by the box model

To further investigate the characteristics of energy transfer in the climate system, especially the heat uptake at the air–sea interface and vertical heat transport in the ocean, under different scenarios, a coupled atmosphere–ocean box model was used in this study. Its simple process can help us understand the nature of energy transportation during the WSP. Its basic idea and equations are discussed in detail in section 3.

Firstly, we simulated the changes of energy transport in the climate system when warming slowdown occurs. The trend of atmospheric temperature in the box model was set as 0.03 °C (10 yr)$^{-1}$ in the low latitudes and 0.08 °C (10 yr)$^{-1}$ in the high latitudes (Table 3) to correspond with results from ERA-Interim (shown in Fig. 3c). The equations of the model are solved numerically using an Euler scheme with 4-day time steps. The model runs for 100 years, and note that all of the results shown below are the perturbation state of the model system. Figure 7 presents the OHC trend in the box model and the observations during the WSP. The result of the bottom layer ocean (2000–4000 m) in the box model is not shown because its temperature changes are relatively small and observations are limited for the ocean below 2000 m. It can be seen from the observation that the OHC in both low- and high-latitude areas shows an obvious positive trend, with an increase of about 5.8 × 10^{21} J yr^{-1} and 3.4 × 10^{21} J yr^{-1}, respectively. For the box model, the simulated patterns of OHC trends in the deeper-layer and upper-layer ocean are quite consistent with the observations (Fig. 7), though their magnitudes are relatively larger. In addition, it is notable that the OHC trend in the deeper layer is larger than its trend in the upper layer, as shown both in the observation and the simulation, indicating more heat storage in the deeper ocean.

The warming patterns in the ocean during the WSP have a tight relationship with the features of energy transport in the climate system, which is also demonstrated in the box model. The OHC changes in the upper ocean are affected by the energy taken into the ocean at the sea surface. Figures 8c and e demonstrate the contribution of related processes to the ocean heat uptake in low latitudes and high latitudes during the warming slowdown scenario, respectively. It is shown that the differences are mainly due to changes in features of energy transport in the cli-

Table 3. Atmospheric temperature trends imposed in the box model.

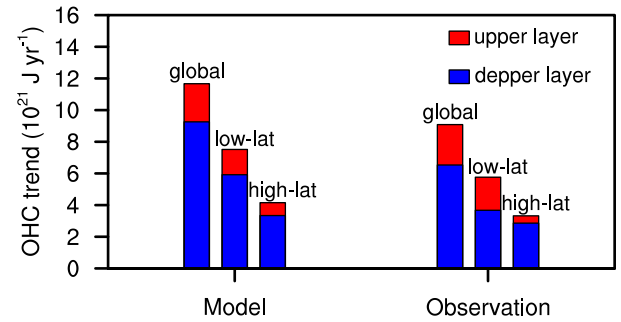|	Warming slowdown scenario	Rapid warming scenario
Low latitudes	0.030 °C (10 yr)$^{-1}$	0.196 °C (10 yr)$^{-1}$
High latitudes	0.080 °C (10 yr)$^{-1}$	0.025 °C (10 yr)$^{-1}$

Fig. 7. OHC trend in the observations and simulation of the box model, from the left to the right representing the global, low-latitude and high-latitude ocean, respectively. The red part represents the upper-layer and the blue part the deeper-layer ocean. The observational OHC is based on the IAP dataset.

mate system, especially the atmospheric heat transport and climate feedback. Because the warming rate of atmospheric temperature in high latitudes is larger than that in low latitudes during the WSP, the meridional atmospheric temperature gradient would be reduced, which would lead to less atmospheric heat transport from the low to high latitudes. As a result, the atmospheric heat transport facilitates the ocean heat uptake in low latitudes, but suppresses it in high latitudes (Figs. 8c and e; green lines). Meanwhile, the higher warming rate in high latitudes means more outgoing longwave radiation (outgoing energy). As a result, the climate feedback has a stronger inhibiting effect on the ocean heat uptake in high latitudes than that in low latitudes (Figs. 8c and e; blue lines). Consequently, the heat uptake and the increased OHC of the upper ocean in high latitudes is less than those in low latitudes during the WSP (Fig. 8a, Fig. 7). As for the deeper (intermediate layer) ocean, the seawater mixing and thermohaline circulation impact the deeper-ocean heat storage. During the WSP, the surface ocean heat uptake in the low latitudes increases faster than that in the high latitudes. As a result, compared with the equilibrium states (all results shown here are perturbation states), the seawater mixing brings more heat from the upper-layer to deeper-layer ocean in low latitudes than in high latitudes (Figs. 9c and e; blue lines), due to a faster increase of temperature gradient. The thermohaline circulation wells up and bring cold water from the bottom layer in the low latitudes, while it conversely sinks in the high latitudes, thus facilitating heat storage in high latitudes and suppressing it in low latitudes (Figs. 9c and e; red line). However, this cannot compensate the differences due to the thermohaline, and eventually, under the concurrent effect of these processes, the heat storage and the increased OHC in low latitudes are larger than those in high latitudes (Fig. 9a, Fig. 7).

Furthermore, we compared the characteristics of OHC

changes between the scenarios of rapid warming and warming slowdown in the box model, by fixing different atmospheric

warming trends for the two scenarios. A faster atmospheric warming trend, about 0.196 °C (10 yr)$^{-1}$ in low latitudes and
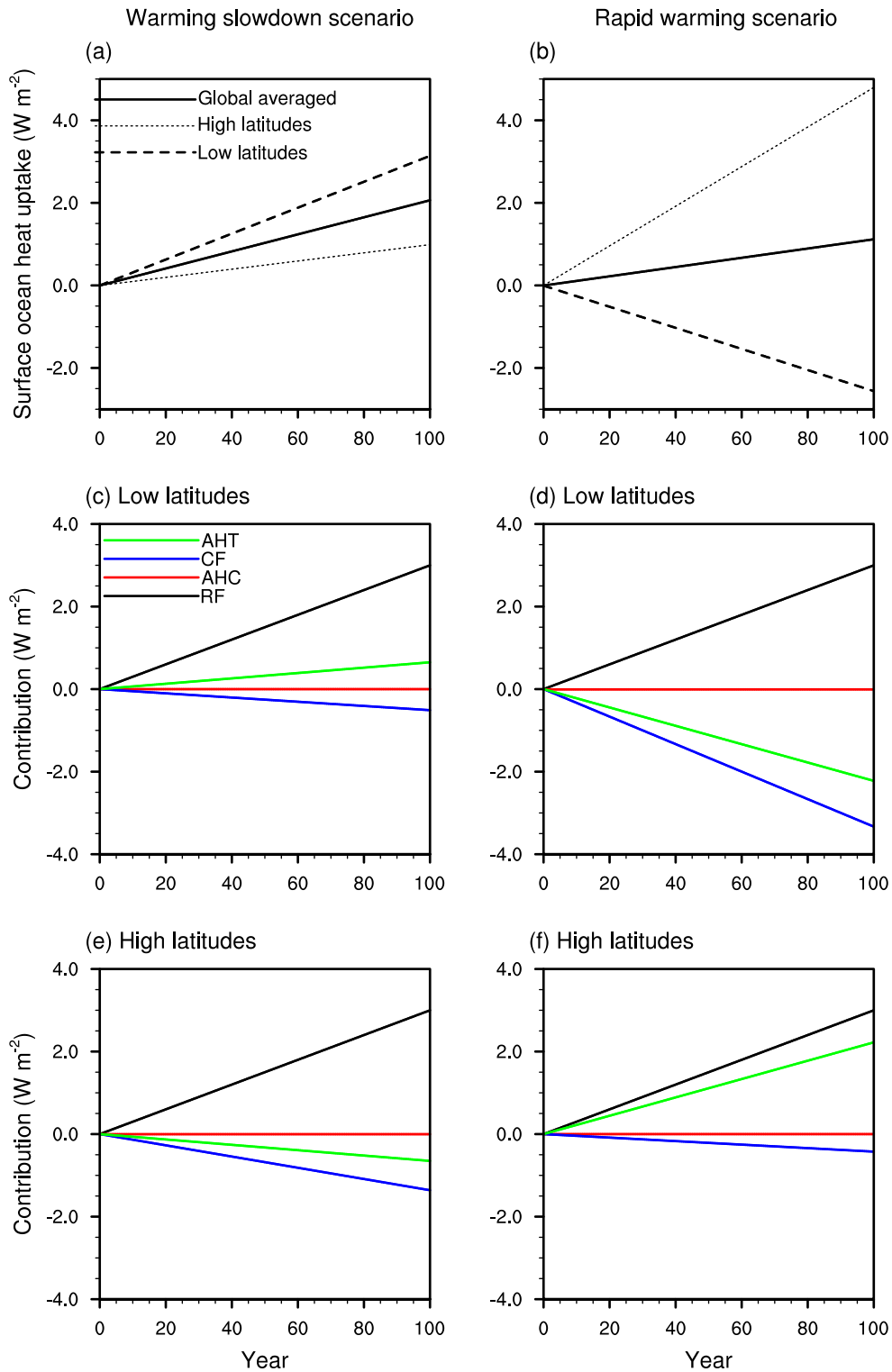

Fig. 8. Ocean heat uptake at the sea surface (a, b) and the contribution of each term to it (c–f) during the warming slowdown scenario (left-hand panels) and rapid warming scenario (right-hand panels). The dashed, dotted and solid lines in (a, b) represent the low-latitude, high-latitude and global-averaged oceans, respectively. The four terms —AHT (green), CF (blue), AHC (red), and RF (black) —in (c –f) represent the atmospheric heat transport, climate feedback, atmospheric heat content, and radiative forcing, respectively. The ocean heat uptake at the surface is equal to the sum of these terms.
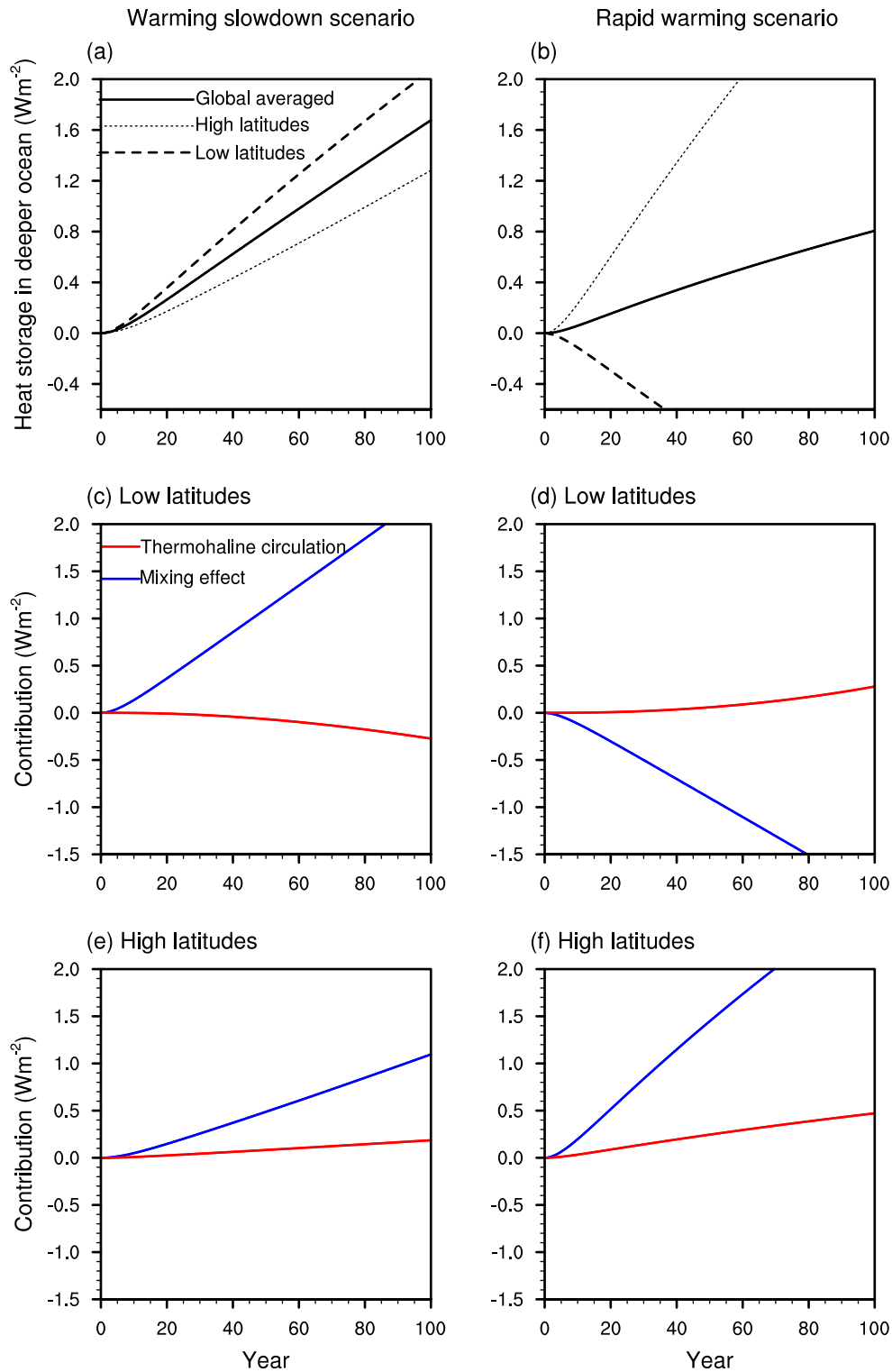
Fig. 9. Heat storage in the deeper-layer (intermediate-layer) ocean (a, b) and the contribution of each term to it (c–f) during the warming slowdown scenario (left-hand panels) and rapid warming scenario (right-hand panels). The dashed, dotted and solid lines in (a, b) represent the low-latitude, high-latitude and global-averaged oceans, respectively. The red and blue lines in (c –f) represent the contributions of the thermohaline circulation and mixing effect, respectively. Heat storage in the deeper-layer ocean in the model is equal to the sum of the two terms.

0.025 °C (10 yr)$^{-1}$ in high latitudes (Table 3), which was also derived from ERA-Interim (shown in Fig. 3c), was set in the box

model to simulate the rapid warming scenario. The simulated OHC difference between the warming slowdown scenario and

the rapid warming scenario is shown in Fig. 10a. It is clear that, compared with the rapid warming scenario, OHC increases faster in both the upper-layer ocean and deeper-layer ocean in the warming slowdown scenario; particularly, the increased OHC in the deeper-layer ocean is greater than that in the upper-layer ocean after several simulated years.The box model ultimately simulates a total OHC trend difference of about 6.2×10^{21} J yr^{-1} between the two scenarios, and the deeper ocean contributes over half of it. This trend difference can be attributed to faster ocean heat uptake at the sea surface and faster deeper-ocean heat storage during the WSP than those during the RWP (Figs. 10b and c). The warming rate of atmospheric temperature in high latitudes is much smaller than that in low latitudes during the RWP, which is opposite to the result during the WSP. Thus, the atmospheric heat transport (Figs. 8d and f; green lines) and climate feedback (Figs. 8d and f; blue lines)

show a much stronger inhibiting effect on the ocean heat uptake in low latitudes than in high latitudes, which are also opposite to the results during the WSP. Consequently, the perturbation of ocean heat uptake at the sea surface in low latitudes is negative, which is far less than that in high latitudes during the RWP (Fig. 8b). It indicates that more heat is transported from the ocean to the atmosphere in low latitudes during the RWP. Thus, the mixing effect shows a strong inhibiting effect on the deeper-ocean heat storage in low latitudes (Fig. 9d; blue line) owing to the reduced temperature gradient between the upper-layer and intermediate-layer ocean—opposite to the situation during the WSP. To compensate, the thermohaline circulation in low latitudes subsequently behaves as a positive effect (Fig. 9d; red line). As for the high latitudes, due to the energy conservation, there would be faster heat transport from the atmosphere to the ocean during the RWP than that during the WSP. Thus,
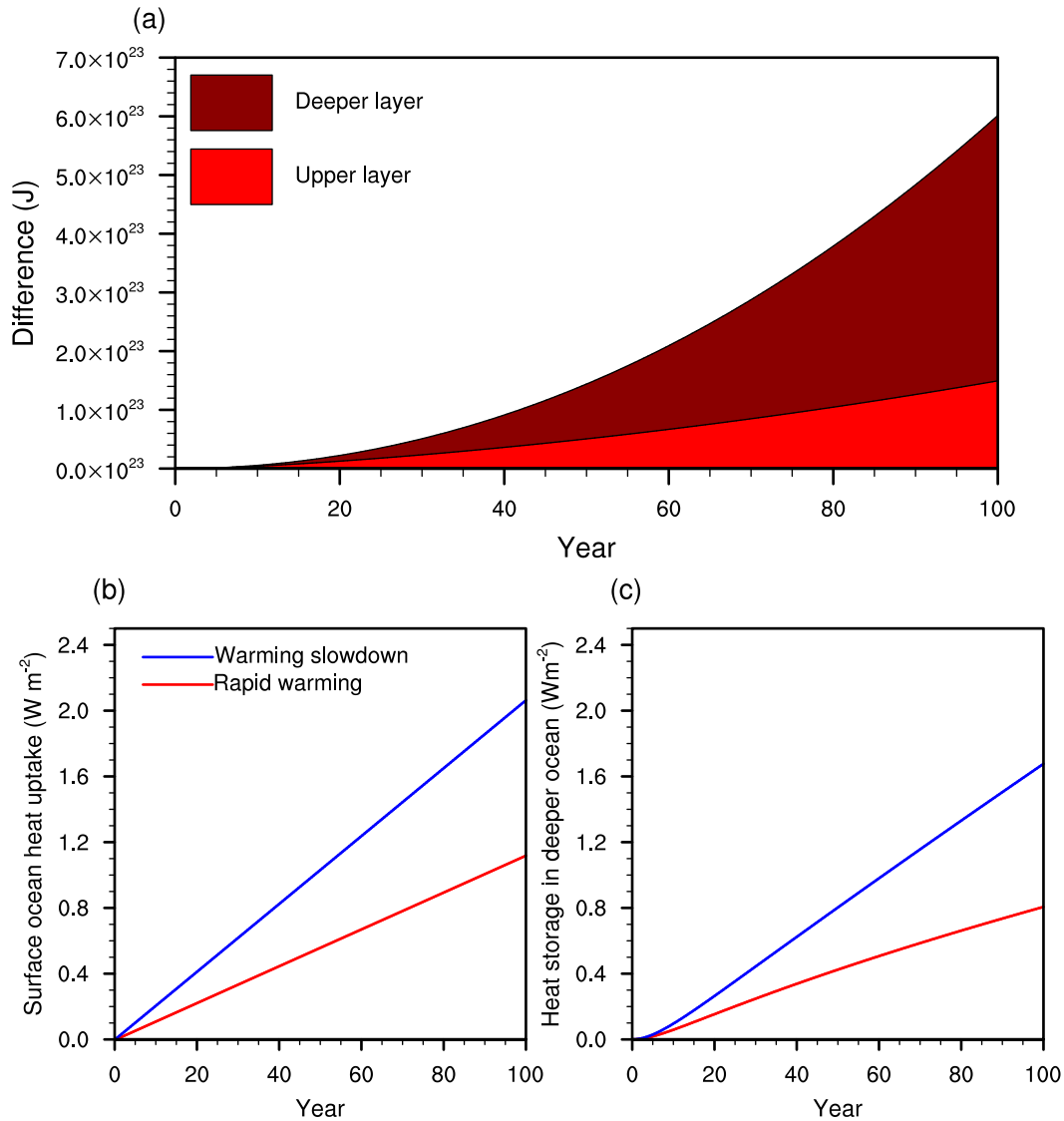

Fig. 10. OHC difference (units: J) between the warming slowdown scenario and the rapid warming scenario (former minus the latter) in the box model (a) and comparison of the global ocean heat uptake at the surface (b) and heat storage in the deeper layer ocean (c) between the two scenarios. The dark red and light red in (a) represent the deeper-layer and upper-layer ocean; the blue line and red line in (b) and (c) represent the warming slowdown scenario and rapid warming scenario, respectively.

both the mixing effect and thermohaline circulation show a moderate facilitating effect on the deeper-ocean heat storage in high latitudes (Fig. 9f). Consequently, for the global ocean (including the low latitudes and high latitudes), the surface ocean heat uptake and the deeper-ocean heat storage during the RWP (Fig. 8b, Fig. 9b, Fig. 10) are both slower than those during the WSP.

6. Summary and discussion

The warming slowdown phenomenon has attracted worldwide attention and has been intensely debated since it was proposed (Easterling and Wehner, 2009; IPCC, 2013). Studies on the warming slowdown have been published since then, and many of them have found a tight link between the warming slowdown and the oceanic energy change (Meehl et al., 2011; Chen and Tung, 2014; Steinman et al., 2015). The importance of the thermohaline circulation has been proposed by several studies, the change of which could influence energy transport in the climate system (Chen and Tung, 2018). However, the physical mechanism of how the ocean energy changes still needs be further explored and clarified.

In this study, we show a distinction between the energy transport in the climate system of the RWP and WSP. Notably, the characteristics of the atmospheric temperature change and the OHC change, as well as the ocean heat uptake, in the low and high latitudes during the WSP are almost opposite to those during the RWP. After removing the substantial anthropogenic warming signal, it can be seen that, during the period of global atmospheric warming slowdown, the global OHC increases faster than that during the period of rapid atmospheric warming. From the global energy balance perspective, we suggest the accelerated ocean heat uptake is tightly coupled with the recent global warming slowdown. Based on the EEMD method, it can be seen that the oscillation component of OHC differs between the WSP and RWP, which indicates the different "drain rate" of energy from the atmosphere to ocean. The upward swing in the oscillation of OHC implies enhancement in ocean heat uptake, thus leading to a downward phase of the atmospheric temperature oscillation, which suppresses the long-term warming trend and finally behaves as a period of atmospheric warming slowdown. Furthermore, EOF analysis showed that the dominant variability of OHC in the upper-layer ocean occurs mainly in the Pacific, while the OHC in the deeper-layer ocean varies mostly in the Atlantic, which reveals the important influence of the thermohaline circulation.

A coupled box model was used in the final part of this study to investigate the characteristics of energy transport in the climate system and confirm the OHC changes under the two scenarios. The model reproduces the accelerated increasing of global OHC under the warming slowdown scenario, the trend of which corresponds well with the results derived from the observational IAP dataset. In particular, the simulated OHC differences presented in Fig. 10 emphasize the important role of the deeper ocean in the warming hiatus, which contributes over half of the total trend differences. Furthermore, the model also revealed that the changes of atmospheric temperature are

tightly linked with the characteristics of air–sea energy transport. Comparing the warming slowdown scenario with the rapid warming scenario, it can be seen clearly that the different atmospheric warming patterns in low/high latitudes under the two scenarios are accompanied by distinct outgoing longwave radiation and atmospheric meridional heat transport, as well as other related processes, thus leading to different characteristics of air–sea heat transport and demonstrating the distinct energy transport in the climate system in the two scenarios.

Some limitations of this study should be acknowledged. The real climate system is extremely complex; neither the simple box model we used (which is oversimplified) nor complex coupled general circulation models (which possess considerable uncertainty) can directly reveal the energy transfer in the atmosphere–ocean system. Therefore, the box model was mainly used to explain some phenomena qualitatively, and not for quantitative analysis. In addition, an accurate heat transport at the sea surface on the decadal time scale remains elusive, due to the large uncertainty (~10 W m^{-2}) in observations of air–sea heat flux (Josey, 2011). Besides, the vertical and inter-basin heat redistribution in the ocean is not well understood, and estimates of OHC from oceanic datasets may be uncertain (Wang et al., 2018). The results presented in this paper are primarily derived from the IAP dataset; however, the characteristics of OHC in the deeper layer of the Indian Ocean seem to be different if other datasets are used, and this may contribute to the uncertainty of estimates of oceanic warming in the low latitudes (Fig. S6). Therefore, this study is just preliminary and heuristic. For a further understanding of the energy transfer in the climate system, more accurate observational datasets and reliable climate models should be developed in the future.

REFERENCES

Balmaseda, M. A., K. Mogensen, and A. T. Weaver, 2013: Evaluation of the ECMWF ocean reanalysis system ORAS4. *Quart.J.Roy.Meteor.Soc.*,**139**(674),1132−1161,https://doi.org/10.1002/qj.2063.

Chen, X. Y., and K. K. Tung, 2014: Varying planetary heat sink led to global-warming slowdown and acceleration. *Science*, **345**(6199), 897−903, https://doi.org/10.1126/science.1254937.

Chen, X. Y., and K. K. Tung, 2018: Global surface warming enhanced by weak Atlantic overturning circulation. *Nature*,

559(7714), 387−391, https://doi.org/10.1038/s41586-018-0320-y.

Cheng, L. J., G. J. Wang, J. P. Abraham, and G. Huang, 2018: Decadal ocean heat redistribution since the late 1990s and its association with key climate modes. *Climate*, **6**, 91, https://doi.org/10.3390/cli6040091.

Cheng, L. J., K. E. Trenberth, M. D. Palmer, J. Zhu, and J. P. Abraham, 2016: Observed and simulated full-depth ocean heat-content changes for 1970-2005. *Ocean Science*, **12**, 925−935, https://doi.org/10.5194/os-12-925-2016.

Cheng, L. J., K. E. Trenberth, J. Fasullo, T. Boyer, J. Abraham, and J. Zhu, 2017: Improved estimates of ocean heat content from 1960 to 2015. *Science Advances*, **3**, e1601545, https://doi.org/10.1126/sciadv.1601545.

Chylek, P., J. D. Klett, G. Lesins, M. K. Dubey, and N. Hengartner, 2014: The Atlantic multidecadal oscillation as a dominant factor of oceanic influence on climate. *Geophys. Res. Lett.*, **41**(5), 1689−1697, https://doi.org/10.1002/2014GL059274.

Dai, A. G., J. C. Fyfe, S. P. Xie, and X. G. Dai, 2015: Decadal modulation of global surface temperature by internal climate variability. *Nature Climate Change*, **5**(6), 555−559, https://doi.org/10.1038/nclimate2605.

Danny Harvey, L. D., and S. H. Schneider, 1985: Transient climate response to external forcing on 10^0-10^4 year time scales part 1: Experiments with globally averaged, coupled, atmosphere and ocean energy balance models. *J. Geophys. Res.*, **90**(D1), 2191−2205, https://doi.org/10.1029/JD090iD01p02191.

Dee, D. P., and Coauthors, 2011: The ERA-interim reanalysis: Configuration and performance of the data assimilation system. *Quart. J. Roy. Meteor. Soc.*, **137**(656), 553−597, https://doi.org/10.1002/qj.828.

Easterling, D. R., and M. F. Wehner, 2009: Is the climate warming or cooling? *Geophys. Res. Lett.*, **36**(8), L08706, https://doi.org/10.1029/2009GL037810.

England, M. H., and Coauthors, 2014: Recent intensification of wind-driven circulation in the pacific and the ongoing warming hiatus. *Nature Climate Change*, **4**(3), 222−227, https://doi.org/10.1038/nclimate2106.

Foster, G., and S. Rahmstorf, 2011: Global temperature evolution 1979-2010. *Environmental Research Letters*, **6**(4), 044022, https://doi.org/10.1088/1748-9326/6/4/044022.

Guan, X. D., J. P. Huang, R. X. Guo, and P. Lin, 2015: The role of dynamically induced variability in the recent warming trend slowdown over the Northern Hemisphere. *Scientific Reports*, **5**, 12669, https://doi.org/10.1038/srep12669.

Hansen, J., R. Ruedy, M. Sato, and K. Lo, 2010: Global surface temperature change. *Rev. Geophys.*, **48**(4), RG4004, https://doi.org/10.1029/2010RG000345.

He, Y. L., J. P. Huang, D. D. Li, Y. K. Xie, G. L. Zhang, Y. L. Qi, S. S. Wang, and S. Totz, 2018: Comparison of the effect of land-sea thermal contrast on interdecadal variations in winter and summer blockings. *Climate Dyn.*, **51**, 1275−1294, https://doi.org/10.1007/s00382-017-3954-9.

Huang, J. P., Y. K. Xie, X. D. Guan, D. D. Li, and F. Ji, 2017: The dynamics of the warming hiatus over the northern hemisphere. *Climate Dyn.*, **48**, 429−446, https://doi.org/10.1007/s00382-016-3085-8.

IPCC, 2013: Summary for policymakers. *Climate Change 2013: The Physical Science Basis*. Contribution of Working Group I to the Fifth Assessment Report of the Intergovernmental Panel on Climate Change. T. F. Stocker et al., Eds., Cambridge University Press, 3--29.

Ji, F., Z. H. Wu, J. P. Huang, and E. P. Chassignet, 2014: Evolution of land surface air temperature trend. *Nature Climate Change*, **4**(6), 462−466, https://doi.org/10.1038/nclimate2223.

Josey, S. A., 2011: Air-sea fluxes of heat, freshwater and momentum. *Operational Oceanography in the 21st Century*, A. Schiller and G. B. Brassington, Eds., Springer, 155--170, https://doi.org/10.1007/978-94-007-0332-2_6.

Kim, K. Y., G. R. North, and J. P. Huang, 1992: On the transient response of a simple coupled climate system. *J. Geophys. Res.*, **97**(D9), 10 069−10 081, https://doi.org/10.1029/92JD00581.

Kosaka, Y., and S. P. Xie, 2013: Recent global-warming hiatus tied to equatorial pacific surface cooling. *Nature*, **501**(7467), 403−407, https://doi.org/10.1038/nature12534.

Krasovskiy, Y. P., and P. H. Stone, 1998: Destabilization of the thermohaline circulation by atmospheric transports: An analytic solution. *J. Climate*, **11**(7), 1803−1811, https://doi.org/10.1175/1520-0442(1998)011<1803:DOTTCB>2.0.CO;2.

Lee, S. K., W. Park, E. van Sebille, M. O. Baringer, C. Z. Wang, D. B. Enfield, S. G. Yeager, and B. P. Kirtman, 2011: What caused the significant increase in Atlantic ocean heat content since the mid-20th century? *Geophys. Res. Lett.*, **38**(17), L17607, https://doi.org/10.1029/2011GL048856.

Lee, S. K., W. Park, M. O. Baringer, A. L. Gordon, B. Huber, and Y. Y. Liu, 2015: Pacific origin of the abrupt increase in Indian Ocean heat content during the warming hiatus. *Nature Geoscience*, **8**(6), 445−449, https://doi.org/10.1038/ngeo2438.

Li, Y. L., W. Q. Han, and L. Zhang, 2017: Enhanced decadal warming of the Southeast Indian Ocean during the recent global surface warming slowdown. *Geophys. Res. Lett.*, **44**, 9876−9884, https://doi.org/10.1002/2017GL075050.

Liu, B., and T. J. Zhou, 2017: Atmospheric footprint of the recent warming slowdown. *Scientific Reports*, **7**, 40947, https://doi.org/10.1038/srep40947.

Marotzke, J., and P. H. Stone, 1995: Atmospheric transports, the thermohaline circulation, and flux adjustments in a simple coupled model. *J. Phys. Oceanogr.*, **25**(6), 1350−1364, https://doi.org/10.1175/1520-0485(1995)025<1350:ATTCA>2.0.CO;2.

Meehl, G. A., J. M. Arblaster, J. T. Fasullo, A. X. Hu, and K. E. Trenberth, 2011: Model-based evidence of deep-ocean heat uptake during surface-temperature hiatus periods. *Nature Climate Change*, **1**(7), 360−364, https://doi.org/10.1038/nclimate1229.

Morantine, M., and R. G. Watts, 1990: Upwelling diffusion climate models: Analytical solutions for radiative and upwelling forcing. *J. Geophys. Res.*, **95**(D6), 7563−7571, https://doi.org/10.1029/JD095iD06p07563.

Morice, C. P., J. J. Kennedy, N. A. Rayner, and P. D. Jones, 2012: Quantifying uncertainties in global and regional temperature change using an ensemble of observational estimates: The HadCRUT4 data set. *J. Geophys. Res.*, **117**(D8), D08101, https://doi.org/10.1029/2011JD017187.

Nakamura, M., P. H. Stone, and J. Marotzke, 1994: Destabilization of the thermohaline circulation by atmospheric eddy transports. *J. Climate*, **7**(12), 1870−1882, https://doi.org/10.1175/1520-0442(1994)007<1870:DOTTCB>2.0.CO;2.

Otterå, O. H., M. Bentsen, H. Drange, and L. L. Suo, 2010: Extern-

al forcing as a metronome for Atlantic multidecadal variability. *Nature Geoscience*, **3**(10), 688–694, https://doi.org/10.1038/ngeo955.

Palmer, M. D., and Coauthors, 2017: Ocean heat content variability and change in an ensemble of ocean reanalyses. *Climate Dyn.*, **49**, 909–930, https://doi.org/10.1007/s00382-015-2801-0.

Rahmstorf, S., 2002: Ocean circulation and climate during the past 120:000 years. *Nature*, **419**(6903), 207–214, https://doi.org/10.1038/nature01090.

Schneider, S. H., and S. L. Thompson, 1981: Atmospheric CO_2 and climate: Importance of the transient response. *J. Geophys. Res.*, **86**(C4), 3135–3147, https://doi.org/10.1029/JC086iC04p03135.

Steinman, B. A., M. E. Mann, and S. K. Miller, 2015: Atlantic and pacific multidecadal oscillations and northern Hemisphere temperatures. *Science*, **347**(6225), 988–991, https://doi.org/10.1126/science.1257856.

Trenberth, K. E., and D. J. Shea, 2006: Atlantic hurricanes and natural variability in 2005. *Geophys. Res. Lett.*, **33**, L12704, https://doi.org/10.1029/2006GL026894.

Trenberth, K. E., and J. Fasullo, 2014b: Earth's energy imbalance. *J. Climate*, **27**(9), 3129–3144, https://doi.org/10.1175/JCLI-D-13-00294.1.

Trenberth, K. E., J. T. Fasullo, G. Branstator, and A. S. Phillips, 2014a: Seasonal aspects of the recent pause in surface warming. *Nature Climate Change*, **4**(10), 911–916, https://doi.org/10.1038/nclimate2341.

von Schuckmann, K., and Coauthors, 2016: An imperative to monitor earth's energy imbalance. *Nature Climate Change*, **6**(2), 138–144, https://doi.org/10.1038/nclimate2876.

Wang, G. J., L. J. Cheng, J. Abraham, and C. Y. Li, 2018: Consensuses and discrepancies of basin-scale ocean heat content changes in different ocean analyses. *Climate Dyn.*, **50**, 2471–2487, https://doi.org/10.1007/s00382-017-3751-5.

Warren, S. G., and S. H. Schneider, 1979: Seasonal simulation as a test for uncertainties in the parameterizations of a Budyko-Sellers zonal climate model. *J. Atmos. Sci.*, **36**(8), 1377–1391, https://doi.org/10.1175/1520-0469(1979)036<1377:SSAATF>2.0.CO;2.

Wu, Z. H., and N. E. Huang, 2009: Ensemble empirical mode decomposition: A noise-assisted data analysis method. *Advances in Adaptive Data Analysis*, **1**, 1–41, https://doi.org/10.1142/S1793536909000047.

Wu, Z. H., N. E. Huang, J. M. Wallace, B. V. Smoliak, and X. Y. Chen, 2011: On the time-varying trend in global-mean surface temperature. *Climate Dyn.*, **37**, 759–773, https://doi.org/10.1007/s00382-011-1128-8.

WMO, 2014: WMO Greenhouse Gas Bulletin: The State of Greenhouse Gases in the Atmosphere Based on Global Observations through 2013. https://library.wmo.int/pmb_ged/ghg-bulletin_10-climate-summit-edition_en.pdf

Wyatt, M. G., S. Kravtsov, and A. A. Tsonis, 2012: Atlantic multidecadal oscillation and northern hemisphere's climate variability. *Climate Dyn.*, **38**, 929–949, https://doi.org/10.1007/s00382-011-1071-8.

Yang, H. J., Y. Y. Zhao, Z. Y. Liu, Q. Li, F. He, and Q. Zhang, 2015: Heat transport compensation in atmosphere and ocean over the past 22:000 years. *Scientific Reports*, **5**, 16661, https://doi.org/10.1038/srep16661.

Yang, H. J., Y. Y. Zhao, and Z. Y. Liu, 2016: Understanding bjerknes compensation in atmosphere and ocean heat transports using a coupled box model. *J. Climate*, **29**, 2145–2160, https://doi.org/10.1175/JCLI-D-15-0281.1.

Yao, S. L., J. J. Luo, G. Huang, and P. F. Wang, 2017: Distinct global warming rates tied to multiple ocean surface temperature changes. *Nature Climate Change*, **7**(7), 486–491, https://doi.org/10.1038/nclimate3304.

Huang, N. E., et al, 1998: The empirical mode decomposition method and the Hilbert spectrum for non-stationary time series analysis. *Proc. R. Soc. Lond. A.*, **454**, 903–995, https://doi.org/10.1098/rspa.1998.0193.

Huang, N. E. &Wu, Z., 2008: A review on Hilbert-Huang transform: the method and its applications on geophysical studies. *Rev. Geophys.*, **46**, RG2006.

Huang, J., Xie, Y., Gu an, X., Li, D. and Ji, F., 2016: The dynamics of the warming hiatus over the northern hemisphere. *Clim. Dyn.*, **48**, 1–18.

Ji, F., Wu, Z., Huang, J. and Chassignet, E. P., 2014: Evolution of land surface air temperature trend. *Nature Climate Change*, **4**, 462–466, https://doi.org/10.1038/nclimate2223.

Wu, Z. &Huang, N. E., 2009: Ensemble empirical mode decomposition: a noise-assisted data analysis method. *Adv. Atmos. Sci.*, **1**, 1–41.

Atmospheric Warming Slowdown during 1998–2013 Associated with Increasing Ocean Heat Content*

Changyu LI, Jianping HUANG, Yongli HE, Dongdong LI, and Lei DING

Key Laboratory for Semi-Arid Climate Change of the Ministry of Education, College of Atmospheric Sciences, Lanzhou
University, Lanzhou, Gansu 730000, China

Ensemble empirical mode decomposition method

The data-analysis method used in section 4 in this study is the ensemble empirical mode decomposition (EEMD) method (Wu and Huang, 2009), which was developed based on the empirical mode decomposition (EMD) method (Huang et al., 1998; Huang and Wu, 2008). EMD is a 1D data-analysis method that is adaptive, has high locality, and can thereby handle the nonlinear and nonstationary nature of data. EEMD adds robustness to the EMD decomposition when data is perturbed by noise, guaranteeing that the physical interpretation of the decomposition result is not sensitive to the noise inevitably contained in real data. In this article, the steps of EEMD are taken from Ji et al. (2014) and Huang et al. (2016), which can be described as follows:

(1) Add a white noise series with an amplitude time (0.2 in this study) that of the standard deviation of the raw data series $x(t)$;

(2.1) Set $x_1(t)=x(t)$ and find the maxima and minima of $x_1(t)$. Then obtain the upper envelope $e_u(t)$ and the lower envelope $e_l(t)$ using cubic splines to connect the maxima and minima, respectively;

(2.2) Find the local mean $m(t) = [e_u(t) + e_l(t)]/2$ and then determine whether $m(t)$ is close to zero at any location based on the given criterion;

(2.3) If yes, stop the sifting process; otherwise, set $x_1(t) = x(t) - m(t)$ and repeat steps 2.1 to 2.2;

(2.4) In this manner, we obtain the first intrinsic mode function (IMF), and by subtracting it from $x(t)$, we obtain a remainder series. If the remainder still contains oscillatory components, we again repeat steps 2.1 to 2.2, but with the new $x_1(t)$ as the remainder.

So, each time series is decomposed into different IMFs, which can be expressed as

$$x(t) = \sum_{j=1}^{n} C_j(t) + R_n(t). \tag{1}$$

where $C_j(t)$ represents the jth IMF, which is an amplitude-frequency-modulated oscillatory component, and $R_n(t)$ is the residual of data $x(t)$, which is either monotonic or contains only one extreme.

(3) Repeat steps 1 and 2 again and again but with different white noise series added each time and obtain the (ensemble) means for corresponding IMFs of the decompositions as the final result.

In the EEMD calculation as outlined in Ji et al. (2014) and Huang et al. (2016), the noise added to data has an amplitude that is 0.2 times the standard deviation of the raw data, and the ensemble number is set to 400.

Sensitivity of the box model to parameter choices

We examined the sensitivity of model under different choices of the parameters, and the results are shown in Fig. S6. Here, we mainly focus on two parameters: the upper-layer water turnover time (τ) and thermohaline mass (V). We changed their values with a range of 0.5–1.5 times relative to the value used in the study. The ratio of the OHC trend difference in the sensitivity experiments to the results in the study is mainly discussed here. It can be seen from Fig. S7, the result in the sensitivity experiments varies due to the changes of the two parameters. However, there is no negative value of the ratio, showing good consistency with the observations and the range of the changes is relatively small, with a maximum ratio of about 1.7 and minimum ratio about 0.6, which is thus acceptable.

REFERENCES

Huang, N. E. *et al*. The empirical mode decomposition method and the Hilbert spectrum for non-stationary time series analysis. *Proc. R. Soc. Lond. A*. **454**, 903–995 (1998).

Huang, N. E. &Wu, Z. A review on Hilbert–Huang transform: the method and its applications on geophysical studies. *Rev. Geophys*. **46**, RG2006 (2008).

Huang, J., Xie, Y., Guan, X., Li, D. and Ji, F. (2016). The dynamics of the warming hiatus over the northern hemisphere. *Clim. Dyn*. **48**, 1-18 (2016).

Ji, F., Wu, Z., Huang, J. and Chassignet, E. P. Evolution of land surface air temperature trend. *Nature Climate Change*, **4**, 462-466 (2014).

Wu, Z. &Huang, N. E. Ensemble empirical mode decomposition: a noise-assisted data analysis method. *Adv. Atmos. Sci*. **1**, 1 –41 (2009).
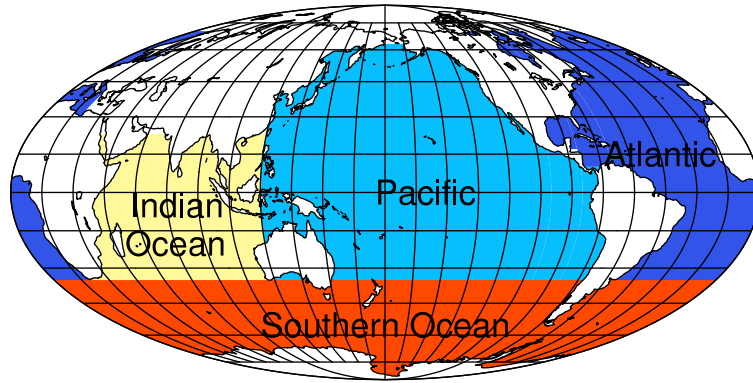
Fig. S1. Division of marine areas. Red, yellow, light blue and dark blue represent the Southern Ocean, Indian Ocean, Pacific Ocean and Atlantic Ocean, respectively.
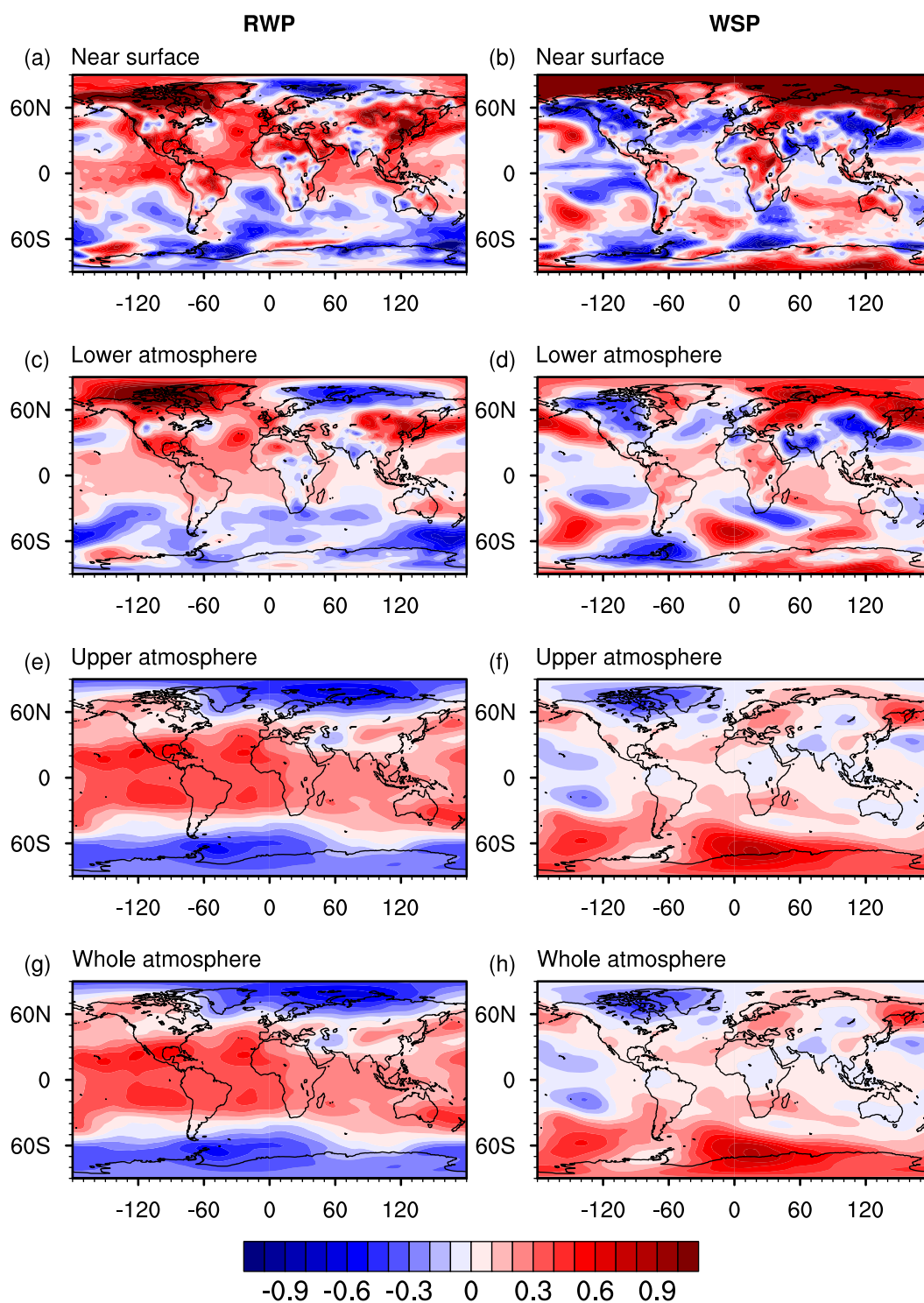
Fig. S2. Trend of atmospheric temperature anomaly [units: °C (10 yr)$^{-1}$] during the RWP (1983–98, left-hand panels) and WSP (1998–2013, right-hand panels). The temperature trend of the near surface (a, b), lower atmosphere (from surface to 500 hPa; c, d), upper atmosphere (from 500 hPa to 100 hPa; e, f) and the whole atmosphere (from surface to 100 hPa; g, h) are shown, respectively.
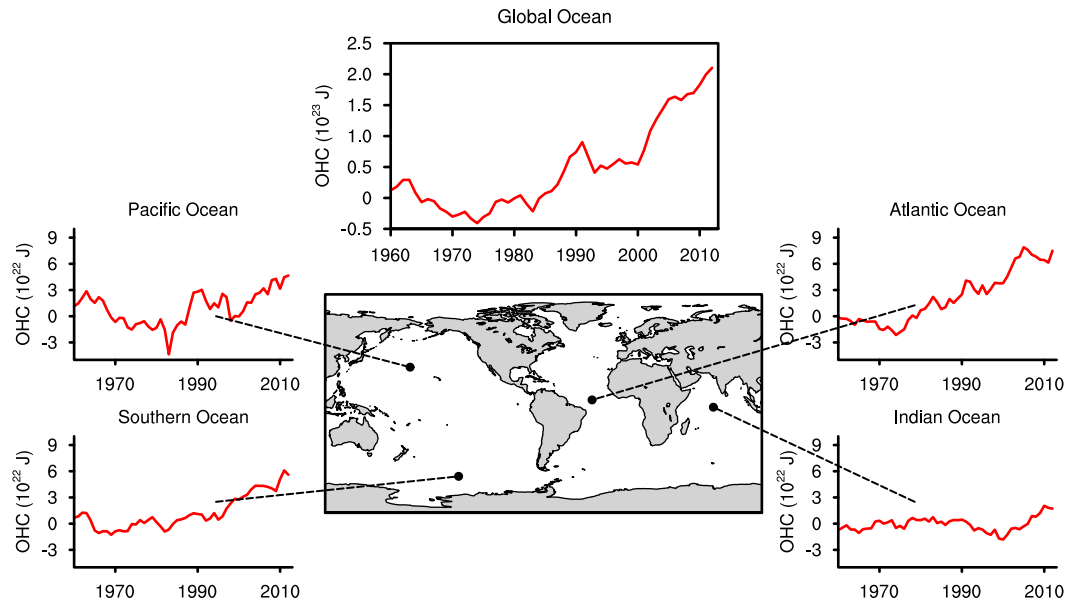
Fig. S3. The OHC anomaly in the global ocean, Atlantic Ocean, Southern Ocean, Pacific Ocean, and Indian Ocean, relative to the climatology from 1961 to 1990. This figure is the same as Fig. 4 but derived from the ORAS4 product.
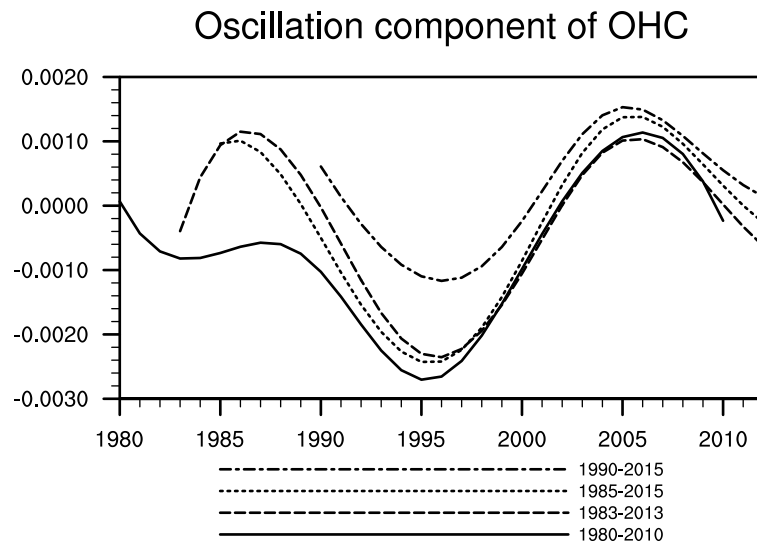

Fig. S4. Oscillation component of OHC under different selected time periods. The periods 1980 –2010, 1983 –2013, 1985 –2015 and 1990 –2015 are examined here.
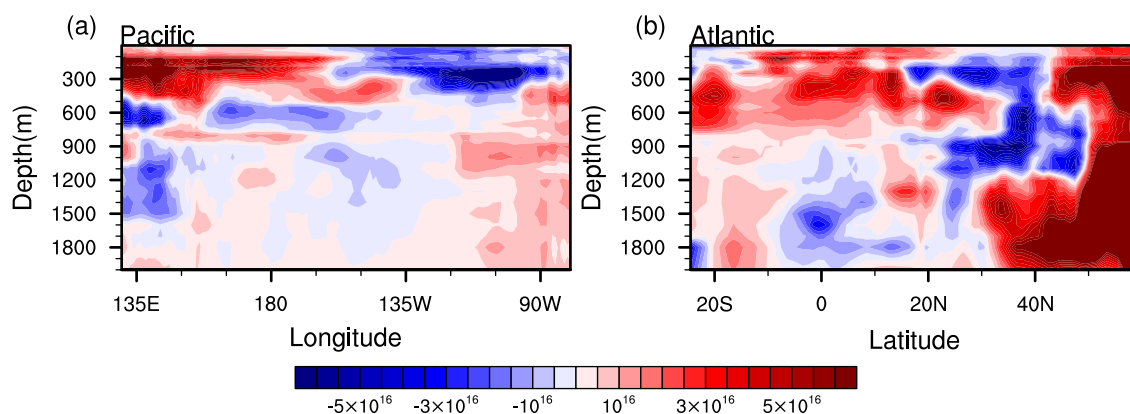
Fig. S5. OHC trend differences between the two periods in the Pacific (a) and Atlantic (b). OHC in the Pacific is meridionally averaged (35°S to 65°N) over the Pacific basin as a function of longitude; OHC in the Atlantic basin is zonally averaged as a function of latitude.
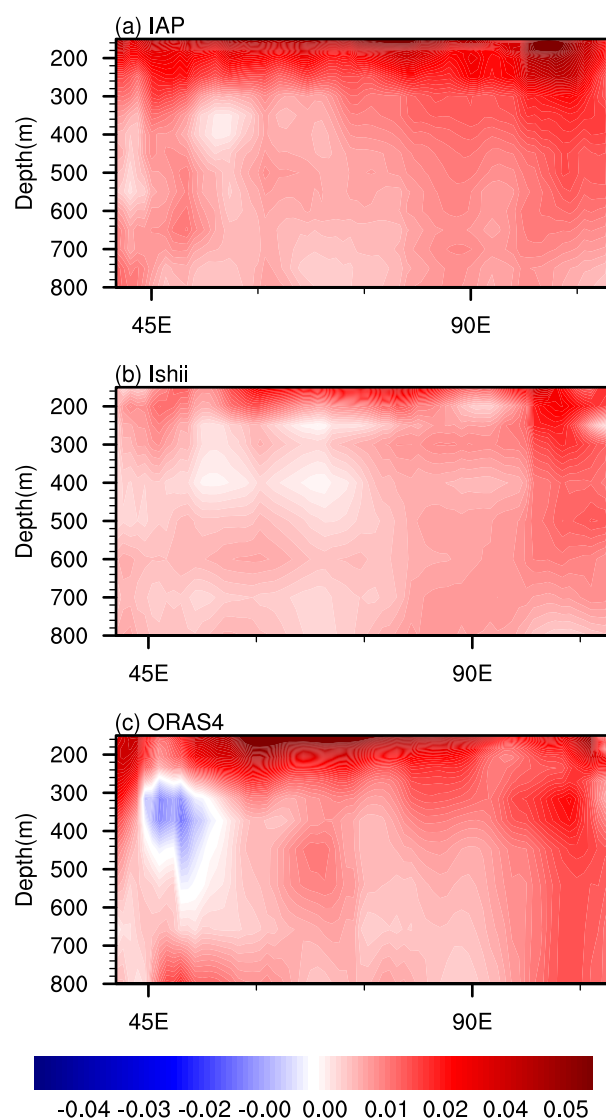

Fig. S6. Seawater temperature trend in the Indian Ocean during the warming slowdown period derived from different datasets. Units: K yr^{-1}.
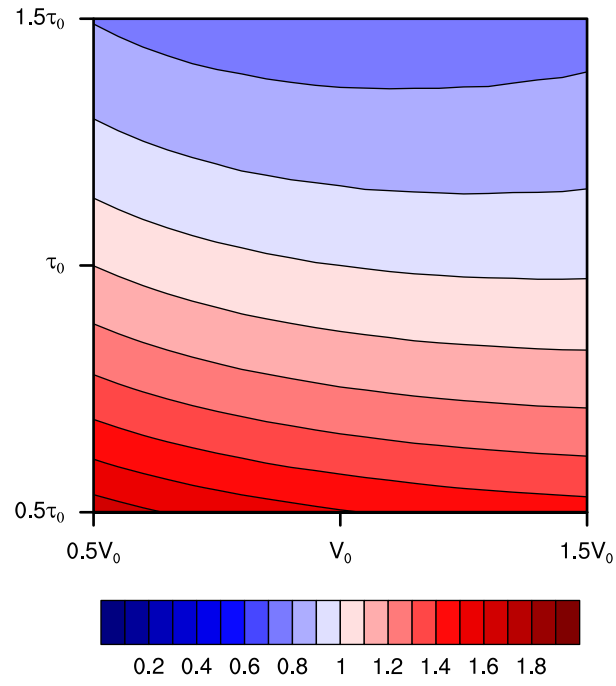
Fig. S7. Sensitivity of the box model to parameter choices: the ratio of OHC trend differences with respect to water turnover time (τ) and thermohaline mass (V).